Article

Mixed Metal Oxide Derived from Polyoxometalate-Based Metal–Organic Framework as a Bi-Functional Heterogeneous Catalyst for Wastewater Treatment

Zi-Qing Liu [1], Jian-Ying Long [2], Xiang Mei [3,*] and Bao-Li Fei [1,4,*]

[1] College of Chemical Engineering, Nanjing Forestry University, Nanjing 210037, China
[2] College of Science, Nanjing Forestry University, Nanjing 210037, China
[3] College of Ecology and Environment, Nanjing Forestry University, Nanjing 210037, China
[4] State Key Laboratory for Chemistry and Molecular Engineering of Medicinal Resources, Guangxi Normal University, Guilin 541004, China
* Correspondence: xiangmei@njfu.edu.cn (X.M.); hgfbl@njfu.edu.cn (B.-L.F.)

Abstract: The efficient removal of dyes and Cr(VI) from wastewater is imperative. Therefore, a mixed metal oxide **CuMoV(450)** derived from a polyoxometalate-based metal–organic framework (POMOF) $[Cu(2,2'-bipy)][Cu(2,2'-bipy)_2]_2[PMo_8V_6O_{42}] \bullet 2H_2O$ (**CuMoV**) was synthesized by calcination, fully characterized by XRD, XPS, FT-IR, and SEM methods, and explored for the heterogeneous catalytic degradation of methylene blue (MB) dye and the catalytic reduction of Cr(VI) in aqueous media over $NaBH_4$ under mild conditions. The removal rates for MB and Cr(VI) were 95.9% (30 min) and 96.5% (2.0 min), respectively. The pseudo-first-order rate constants of MB degradation and Cr(VI) reduction were 0.093 min^{-1} and 1.536 min^{-1}, respectively. The highly catalytic reusability of **CuMoV(450)** was confirmed by the recycling experiments. Moreover, the possible mechanisms of MB degradation and Cr(VI) reduction were proposed. The catalytic activities of **CuMoV(450)** were much better than those of its parent compound **CuMoV**, proving that POMOFs were good candidates for the preparation of mixed metal oxides with excellent catalytic performances. This work not only indicates that **CuMoV(450)** has the potential to be a satisfied catalyst for wastewater remediation via catalytic degradation and reduction, but also gives a clue to synthesize mixed metal oxides with excellent catalytic properties by the calcination of POMOFs.

Keywords: MB degradation; Cr(VI) reduction; mixed metal oxide; POMOFs

1. Introduction

Developing novel efficient technology to deal with wastewater containing various dyes including methylene blue (MB) is urgent, because such wastewater can bring about serious environmental and health problems. So far, a series of physical, chemical, and biological techniques, such as adsorption, photocatalysis, electrochemical degradation, biodegradation, and Fenton reaction, have been used to address the issue of dye wastewater treatment [1]. However, these techniques often require complex procedures, external energy, and stimulants [1]. Hence, exploring other simple and effective processes for dye wastewater treatment is more desirable in the field of environmental remediation.

Industrial wastewater with heavy metals composition is another source of water pollution [2]. Hexavalent chromium Cr(VI) is one of the most dangerous and ubiquitous metal environmental pollutants, which is highly toxic and carcinogenic to various living

organisms [2]. Till now, adsorption, reduction, chemical precipitation, and membrane filtration and photocatalytic technology methods have been explored to remove Cr(VI) [2,3]. Among the various methods employed, the chemical reduction of Cr(VI) to Cr(III) was the most preferred and widely studied, because Cr(III) is relatively inert and non-toxic and a micro-nutrient for the human body [2,4]. To date, the dominant reductive catalysts are noble metal nanoparticles (NPs) [5]. It is an urgent task to find a noble-metal-free catalyst with high catalytic reduction activity because noble metals are too rare to be practically applied as catalysts.

Recently, heterogeneous catalysis, which can degrade organic pollutants including dyes under ambient conditions, has been regarded as a potential method to deal with dye wastewater [1]. This type of chemical catalysis is of great interest due to the easy operation without external energy or chemical stimulants. But reports about the degradation of environmental contaminants under ambient conditions are rare [6].

Metal oxides have been widely used in heterogeneous catalysis, energy storage and conversion, sensors, and biomedical fields [7]. Desirable metal oxides are expected to oxidize and remove organic compounds in the dark without adding external energy and chemical stimulants [6]. Metal oxides, especially perovskites with the formula of ABO_3, are the most studied mixed oxides in heterogeneous catalysis [6,8]. But it is necessary to search for other types of catalysts due to the formation of a carbonate phase on perovskites and the structural collapse during the reaction [8].

Polyoxometalates (POMs) are a special class of metal (Mo^V, Mo^{VI}, Nb^V, Ta^V, V^V, and W^{VI}) oxide polyanion clusters with highly tunable functional characteristics, ranging in size from nanometer to micrometer, and they are explored in various areas such as medicine, catalysis, and electrochemistry [9]. POMs are excellent precursors to prepare well-dispersed, nanoscale, and porous metal composites, such as multi-metallic oxides and carbides [10].

Metal–organic frameworks (MOFs) are crystalline porous compounds composed of covalently bonded metal ions or metal clusters and organic ligands [11]. POM-based metal–organic frameworks (POMOFs) are composed of POM units and metal–organic fragments. POMOFs were usually synthesized by the self-assembly of POM precursors or simple salts, metal ions, and organic ligands under hydro-/solvo-/iono-thermal conditions or a conventional aqueous solution [12]. POMOFs integrate the advantages of both POMs and MOFs.

POMOFs have been widely investigated in the fields of acid catalysis, oxidation catalysis, photocatalysis, electrocatalysis, and others [12]. POMs are one branch of metal oxides, and thus POMOFs can be carbonized to obtain chemically doped porous carbon-coated nanosized transition-metal (Mo, W, V from POM) oxides or carbides. Lin et al. first synthesized MoO_3@CuO material using the POMOFs precursor through a pyrolysis route [13]. Yu et al. prepared the MoO_2@PC-RGO hybrid material from POMOFs/GO composite at a relatively low carbonization temperature [14]. The works of Lin and Yu prove that POMOFs could be transformed into metal oxides by calcination. In recent years, metal oxides as catalysts for the removal of wastewater pollutants have attracted extensive attention in the research community [15,16]. Metal nano-oxides formed by the elements titanium (Ti), manganese (Mn), copper (Cu), and zinc (Zn) with oxygen were obtained [10]. Mixed metal oxides exhibit more unique physicochemical properties than single metal oxides. The high specific surface area and excellent catalytic activity of mixed metal oxides were important for wastewater treatment [10]. Liu et al. prepared porous $MnFe_2O_4$ and $CoFe_2O_4$ nanocomposites to degrade MB with an efficiency of 99.7% [1]. Bhatia et al. synthesized ternary metal oxides Ag_2O/NiO/ZnO to effectively catalyze the reduction of a variety of nitro phenols, dyes, and their mixtures [12].

The advantage of using POMOFs as precursors is that their pyrolysis products normally incorporate at least two metal oxide components with ideal dispersing homogeneity [11]. Literature research indicates that no mixed metal oxides derived from POMOFs were used in heterogeneous catalysis for the degradation of dye and catalytic reduction of Cr(VI) to Cr(III).

Inspired by the previous works, a POMOF precursor [Cu(2,2′-bipy)][Cu(2,2′-bipy)$_2$]$_2$ [PMo$^{VI}_8$V$_1^V$V$_3^{IV}$O$_{40}$(V^{IV}O)$_2$]•2H$_2$O (**CuMoV**) was synthesized by hydrothermal technique. The target mixed metal oxide **CuMoV(450)** was obtained by the calcination of **CuMoV** at 450 °C. **CuMoV(450)** was studied as a heterogeneous catalyst for the removal of MB and Cr(VI). This is the first report about the dye and Cr(VI) removal performance of mixed metal oxides originating from POMOF. The results of this work provide the foundation for the development of mixed metal oxides arising from POMOFs as catalysts for the practical application of environmental remediation.

2. Results and Discussion

2.1. Characterization of *CuMoV* and *CuMoV(450)*

TG measurement was carried out to investigate the effect of calcination on the structure of **CuMoV**. The TG curve of **CuMoV** shows that the initial weight loss of 1.29% up to 310 °C was caused by the loss of six crystal water molecules; afterward, the rapid weight loss of 27.83% was due to the decomposition and extraction of 2,2′-bipy ligands up to 420 °C (Figure S1) [17]. Lastly, the POM sub-unit began to decompose above 450 °C [18]. The TG results confirm that the calcination temperature of 450 °C was enough to prepare mixed metal oxides.

The successful synthesis of **CuMoV** was solidified as shown in Figure S2. It can be seen that the XRD pattern of the prepared **CuMoV** was consistent with the simulated one according to CIF files (CCDC number: 656018), verifying that the **CuMoV** sample kept the single-crystal structure. The characteristic diffraction peaks of Keggin type POM unit appeared at 8.04° (1 0 0), 10.46° (1 1 1) and 19.56° (0 2 2), respectively [19]. Figure 1a displays that the XRD patterns of **CuMoV** and its calcined product **CuMoV(450)** were different. Figure 1b states that **CuMoV(450)** was composed of V$_2$O$_5$, VO$_2$, α-MoO$_3$, CuMoO$_4$, (VO)MoO$_4$, and Cu$_3$(PO$_4$)$_2$. The diffraction peak located at 21.79° corresponded to the (1 1 0) crystal plane of V$_2$O$_5$ (PDF no. 76-1803). The diffraction peaks of VO$_2$ (PDF no. 76-0673) were mainly distributed at 36.80° (−1 1 1) and 41.70° (−2 2 1). The peaks of α-MoO$_3$ (PDF no. 05-0508) were located at 38.58° (1 3 1) and 42.38° (1 4 1) [13]. The diffraction peaks CuMoO$_4$ (PDF no. 89-0228 were located at 25.08° (0 1 2), 29.30° (−1 −2 2), and 43.44° (1 −3 3), respectively [13]. Diffraction peaks were also observed for the mixtures (VO)MoO$_4$ (PDF no. 74-1508), Cu$_3$(PO$_4$)$_2$ (PDF no. 70-0494) at 26.96° (2 0 0), 28.31° (1 1 1), and 30.55° (0 1 2), and 32.20° (−1 1 0), respectively [20].

The FT-IR spectra of **CuMoV** and **CuMoV(450)** are shown in Figure 2. The FT-IR spectrum of **CuMoV** displays the characteristic peaks of the Keggin unit generated by (M-O)(M=Mo/V) (731 cm^{-1}, 789 cm^{-1}, and 937 cm^{-1}), and P-O stretching vibrations (1030 cm^{-1} and 1050 cm^{-1}), respectively. The series peaks in the range of 1100 cm^{-1}– 1600 cm^{-1} were attributed to the 2,2′-bipyridine ligand [21]. No peaks of the Keggin unit and 2,2′-bipyridine appeared in the FT-IR spectrum of **CuMoV(450)**. Instead, the peaks derived from Cu-O, V-O-V, and V=O bonds were found at 613 cm^{-1}, 770 cm^{-1}, and 1053 cm^{-1}, respectively [22,23]. The peaks at 871 cm^{-1} and 960 cm^{-1} belonged to the Mo=O bond in MoO$_3$ [24]. The peaks at 745 cm^{-1} and 1112 cm^{-1} corresponded to the stretching vibration of ν$_{as}$(O-P-O) [25].
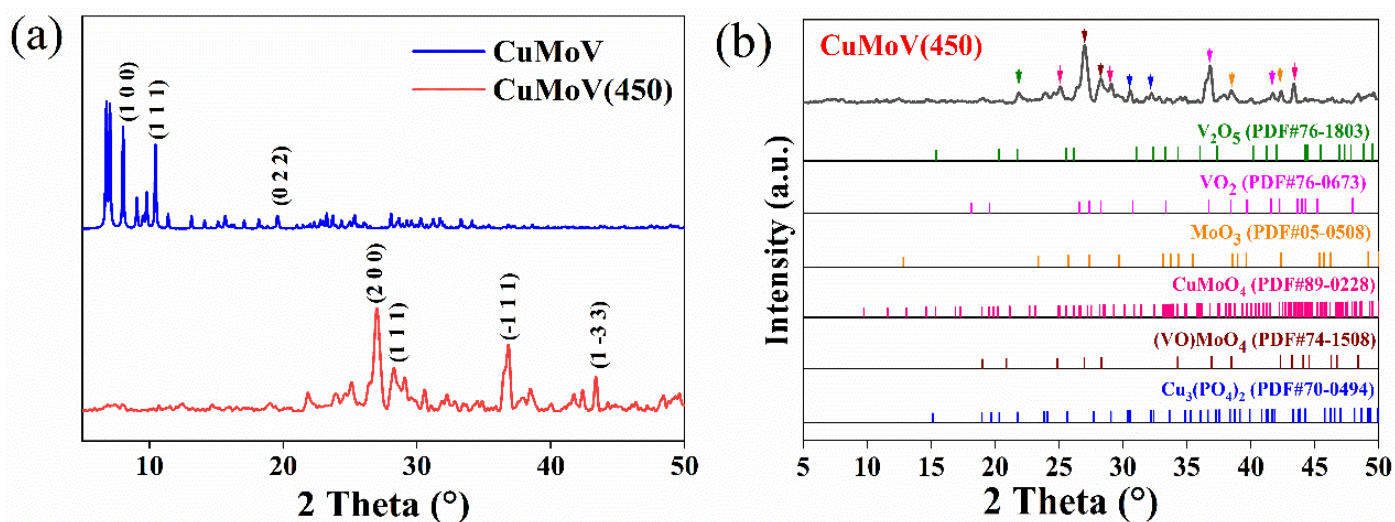
Figure 1. (**a**) XRD patterns of **CuMoV** and **CuMoV(450)**. (**b**) Analysis of XRD patterns of **Cu-MoV(450)**.
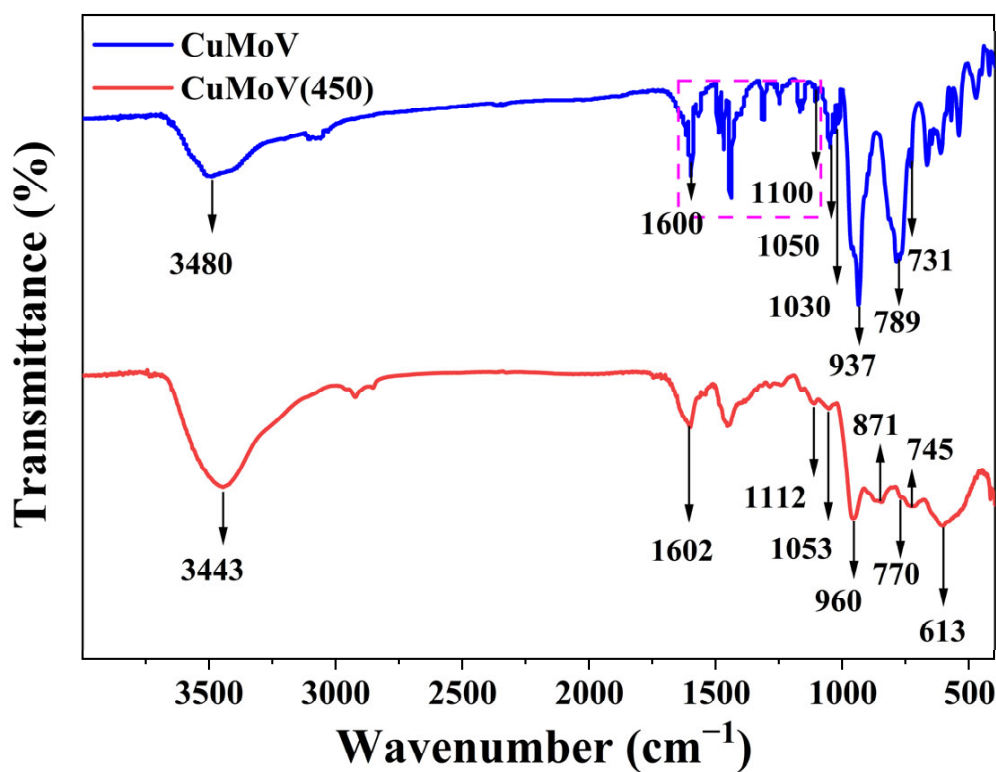
Figure 2. FT-IR spectra of **CuMoV** and **CuMoV(450)**.

SEM analysis was carried out to check the effect of calcination on the morphology of **CuMoV**. Figure 3a shows that the morphology of **CuMoV** was block in shape, and the surface of **CuMoV** was smooth. Figure 3b reveals that the calcination promoted the partial collapse of the block morphology and the generation of the surface pores.
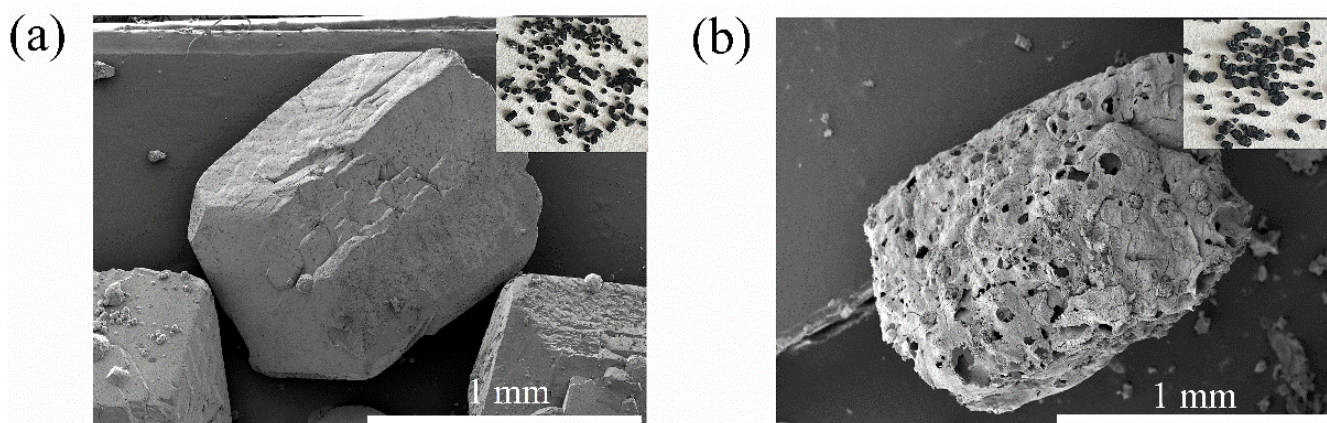
Figure 3. SEM images of **CuMoV** (**a**) and **CuMoV(450)** (**b**).

The chemical purity and stoichiometry of **CuMoV** and **CuMoV(450)** were also investigated by EDX analysis (Figure S3). The EDX spectra indicate the presence of C, N, P, Mo, O, V, and Cu elements in **CuMoV**, and **CuMoV(450)** was composed of P, Mo, O, V and Cu elements.

XPS analysis was performed to determine the elemental composition and chemical valences of **CuMoV** and **CuMoV(450)**. The survey spectra given in Figure 4a suggest that both **CuMoV** and **CuMoV(450)** contained P, Mo, O, V, and Cu elements. The high-resolution XPS spectra of O 1s, P 2p, Cu 2p, Mo 3d, and V 2p are shown in Figure 4b–f. The O 1s spectrum shows three peaks with binding energy at 530.4 eV, 530.8 eV, and 531.6 eV, corresponding to O-V/O-Mo, O-P, and O-Cu bonds, respectively (Figure 4b) [26–28]. The peaks observed at 133.1 eV and 133.4 eV in the P 2p spectrum were attributed to the P-O bond (Figure 4c). There were some differences in the Cu 2p spectra of **CuMoV** and **CuMoV(450),** as indicated in Figure 4d. For **CuMoV**, the peaks corresponding to Cu $2p_{3/2}$ and Cu $2p_{1/2}$ of Cu^{2+} were located at 934.4 eV and 954.2 eV, respectively, with satellite peaks at 943.2 eV and 962.7 eV [29,30]. For **CuMoV(450)**, the corresponding peaks were slightly shifted to 935.0 eV and 954.8 eV due to the existence of CuO. There were also differences in the Mo 3d spectra of **CuMoV** and **CuMoV(450)** (Figure 4e). For **CuMoV**, the two peaks that appeared at 232.3 eV and 235.4 eV belonged to Mo $3d_{5/2}$ and Mo $3d_{3/2}$ of Mo^{6+}, respectively [31]. For **CuMoV(450)**, the peaks attributed to Mo $3d_{5/2}$ and Mo $3d_{3/2}$ of Mo^{6+} were located at 232.8 eV and 236.0 eV, and the peaks assigned to Mo^{5+} were appeared at 232.4 eV and 235.1 eV. The existence of Mo^{5+} might be due to the capture of the trace oxygen vacancies during calcination by Mo^{6+} [32]. The V 2p spectra of **CuMoV** and **CuMoV(450)** in Figure 4f were basically the same. The peaks near 516 eV and 523 eV were assigned to V $2p_{3/2}$ and V $2p_{1/2}$ of V^{4+}, and the peaks near 517 eV and 524 eV were assigned to V $2p_{3/2}$ and V $2p_{1/2}$ of V^{5+}, respectively [33]. The binding energy, weight ratio, and atomic ratio of the above-mentioned elements for **CuMoV** and **CuMoV(450)** are listed in Table S1.
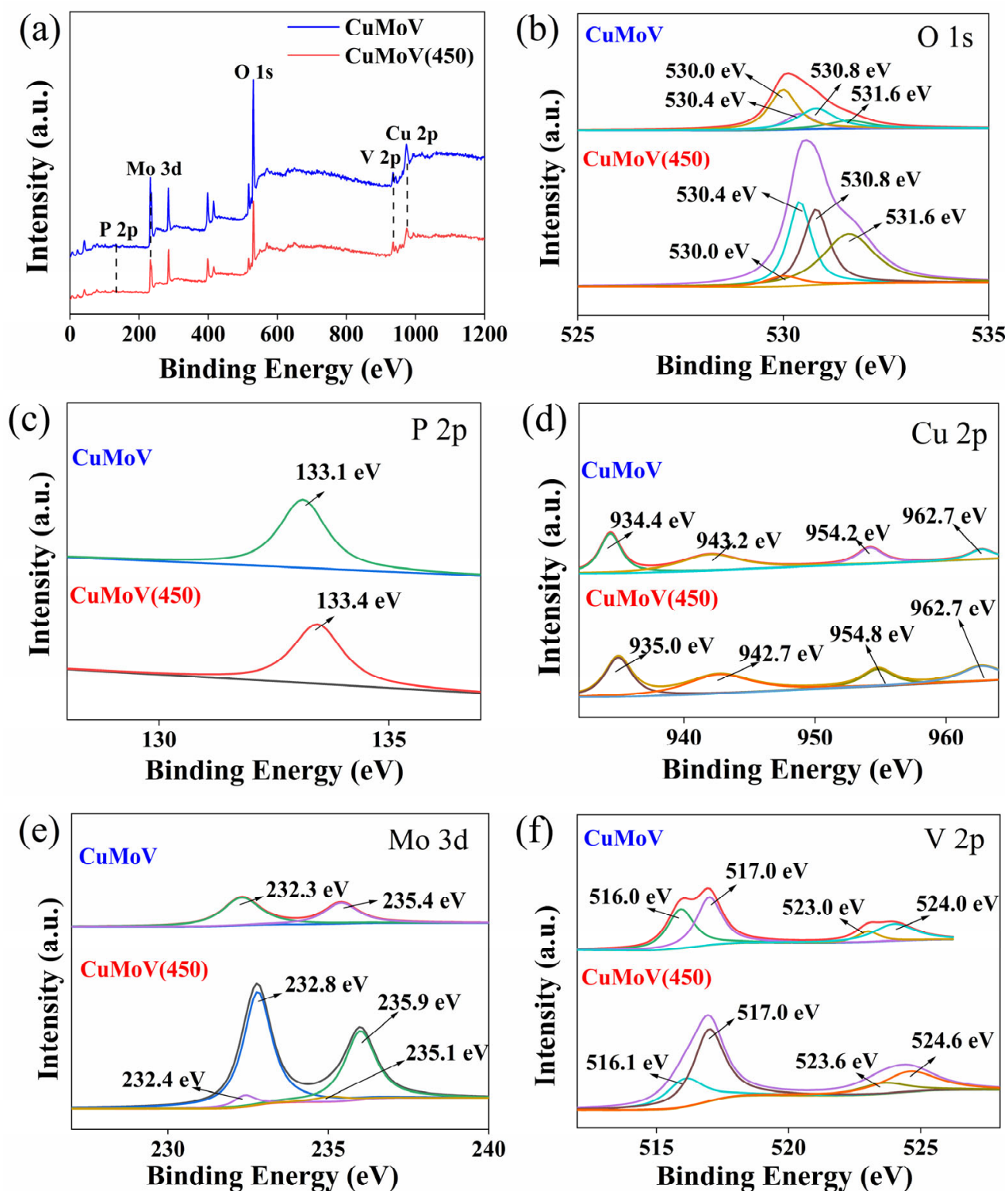
Figure 4. XPS spectra of **CuMoV** and **CuMoV(450)**: (**a**) survey spectra; (**b**) O 1 s; (**c**) P 2p; (**d**) Cu 2p; (**e**) Mo 3d; (**f**) V2p.

2.2. Degradation of MB

The heterogeneous catalytic activities of **CuMoV(450)** were evaluated through MB degradation, and **CuMoV** was used as a positive control. The MB degradation rates were 41.6% (**CuMoV**) and 95.9% (**CuMoV(450)**) in 30 min, respectively, and MB itself could not degrade under the same conditions (Figure 5a). It is evident that the catalytic activities of

CuMoV(450) were far superior to that of **CuMoV**. Consequently, the following research was focused on **CuMoV(450)**.
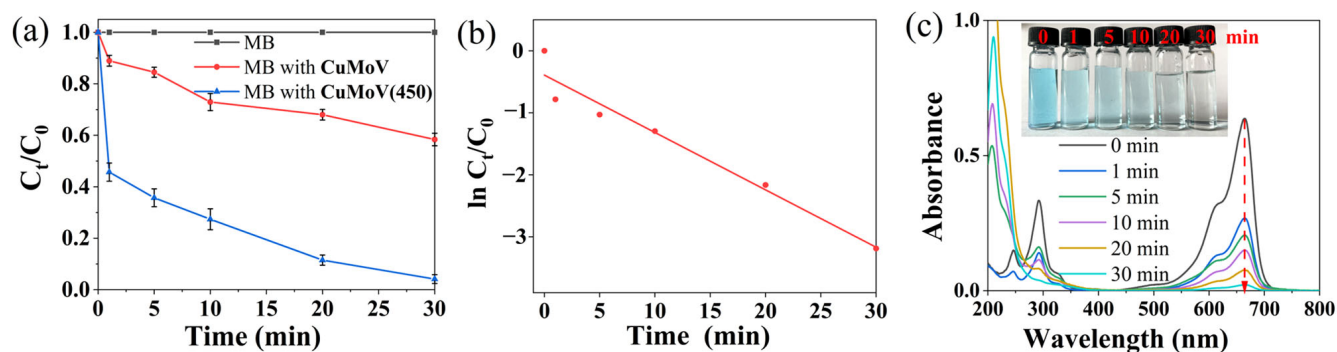
Figure 5. (**a**) Control experiments of MB degradation in 30 min, (**b**) ln (C_t/C_0) as a function of time (t) for MB degradation in 30 min, (**c**) Changes in absorption spectra of MB solution during the degradation process. **CuMoV(450)** dosage = 80 mg, [MB] = 0.01 mM (50 mL), [pH] = 6.8.

The dosage of **CuMoV(450)**, the initial pH value of the MB solution, and the concentration of the MB solution all had a certain effect on MB degradation, and the corresponding results are illustrated in Figure S4. Figure 5b represents the plot of ln (C_t/C_0) against time under the optimum conditions (0.01 mM MB, pH = 6.8, 80 mg **CuMoV(450)**). The calculated values of the rate constants K_{app} and R^2 were 0.093 min^{-1} and 0.955, respectively, confirming that MB degradation obeyed the pseudo-first-order reaction kinetics. The slight deviation of the linear fitting was caused by the different intervals of sampling time. The color of the MB solution changed from blue to colorless in 30 min, and the intensity of the characteristic peaks of MB at 292 nm and 664 nm gradually decreased they until disappeared, demonstrating that the MB molecule was degraded (Figure 5c).

To find the key reactive oxygen species (ROS) responsible for MB degradation, different radical scavengers were added to the reaction system. 1,4-benzoquinone (p-BQ), isopropanol (IPA), and L-histidine were used as $^{\bullet}O_2H/^{\bullet}O_2{}^-$, $^{\bullet}OH$, and $^1O_2$ scavengers, respectively [1,34].

The inhibitory effect of the added scavengers on MB degradation was in the following order IPA > L-histidine > p-BQ (Figure 6a). That is to say, all the examined active species played roles in MB degradation and followed the order of $^{\bullet}OH > {}^1O_2 > {}^{\bullet}O_2{}^-/^{\bullet}O_2H$, and the $^{\bullet}OH$ radical was the most dominant. Furthermore, $^{\bullet}OH$-trapping photoluminescence (PL) spectra of the system in terephthalic acid (TA) solution were measured to confirm the formation of $^{\bullet}OH$ radicals (Figure 6b) [35]. $^{\bullet}OH$ can react with non-fluorescent TA to form highly fluorescent 2-hydroxyterephthalic acid [35]. The PL emission peak of the system in TA solution (0.5 M NaOH, 0.5 mM TA) at 425 nm stemmed from 2-hydroxyterephthalic acid increased with prolonging time, suggesting that the yield of $^{\bullet}OH$ radicals increased over time during MB degradation.

Based on the above results, a possible MB degradation mechanism was proposed [36,37]. MB molecules firstly donated electrons into **CuMoV(450)** via active V^{5+} and Mo^{6+} (Equations (1) and (2)), then the generated V^{4+} and Mo^{5+} reacted with dissolved O$_2$ to give birth to $^{\bullet}O_2{}^-$ (Equations (4) and (5)), and the further reaction of $^{\bullet}O_2{}^-$ produced diverse reactive oxygen species (Equations (6)–(8)). The possible reduction of Mo^{6+} by V^{4+} in Equation (3) might contribute to the increased production of e$^-$ and $^{\bullet}O_2{}^-$, and thus boost the degradation rate. More $^{\bullet}OH$ radicals might be generated as shown in Equations (9) and (10). The disproportionation of $^{\bullet}OH$ radicals should con-

tribute to the yield of $^1O_2$ (Equation (11)) [38]. Ultimately, MB/MB$^+$ was degraded by $^\bullet OH/^\bullet O_2^-/HO_2^\bullet/^1O_2$ (Equation (12)).

$$\equiv V^{5+} + MB \rightarrow \equiv V^{4+} + MB^+ + e^- \tag{1}$$

$$\equiv Mo^{6+} + MB \rightarrow \equiv Mo^{5+} + MB^+ + e^- \tag{2}$$

$$\equiv Mo^{6+} + \equiv V^{4+} \leftrightarrow \equiv Mo^{5+} + \equiv V^{5+} \tag{3}$$

$$\equiv V^{4+} + O_2 \rightarrow {}^\bullet O_2^- + \equiv V^{5+} \tag{4}$$

$$\equiv Mo^{5+} + O_2 \rightarrow {}^\bullet O_2^- + \equiv Mo^{6+} \tag{5}$$

$${}^\bullet O_2^- + H^+ \rightarrow HO_2{}^\bullet \tag{6}$$

$$2HO_2{}^\bullet \leftrightarrow O_2 + H_2O_2 \tag{7}$$

$${}^\bullet O_2^- + H_2O_2 \rightarrow O_2 + {}^\bullet OH + OH^- \tag{8}$$

$$H_2O_2 + \equiv V^{4+} \rightarrow OH^- + {}^\bullet OH + \equiv V^{5+} \tag{9}$$

$$H_2O_2 + \equiv Mo^{5+} \rightarrow OH^- + {}^\bullet OH + \equiv Mo^{6+} \tag{10}$$

$$4{}^\bullet OH \rightarrow {}^1O_2 + 2H_2O \tag{11}$$

$$MB/MB^+ + {}^\bullet OH/{}^\bullet O_2^-/HO_2{}^\bullet/{}^1O_2 \rightarrow \text{degradation products} \tag{12}$$
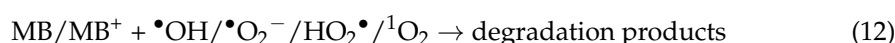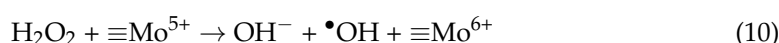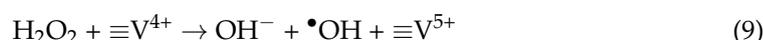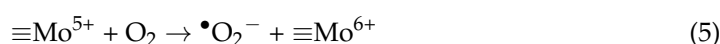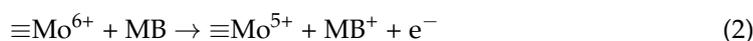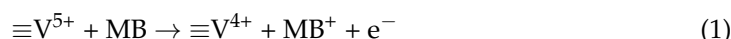
The MB degradation intermediates were analyzed by the HPLC-MS technique. Twelve intermediates with m/z of 261, 249, 227, 198, 195, 174, 163, 157, 102, 106, 130, and 145 were found during the degradation process (Figure 7a). Such results imply that demethylation, deamination, and ring-opening reactions occurred during MB degradation [39,40]. The above analysis leads to the speculation of a possible degradation pathway of MB (Figure 7b).
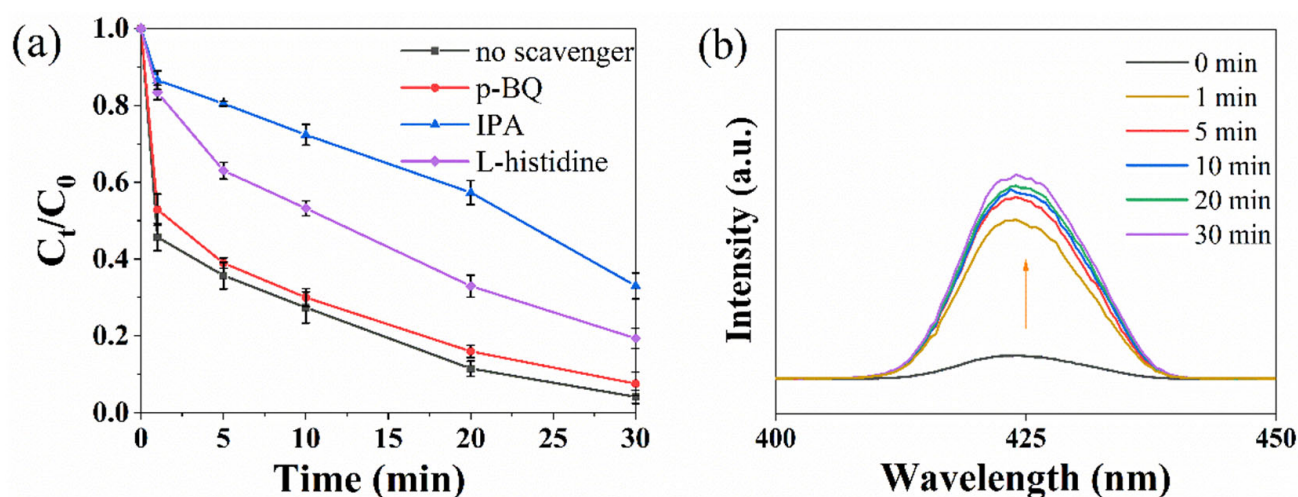
Figure 6. (**a**) Effect of different scavengers on MB degradation. (**b**) PL spectra of TAOH solutions in **CuMoV(450)**/MB system. **CuMoV(450)** dosage = 80 mg, [MB] = 0.01 mM (50 mL), [pH] = 6.8, [p-BQ] = 5 mM, [IPA] = 0.1 M, [L-histidine] = 0.1 M, [TAOH] = 0.5M NaOH + 0.5 mM TA.
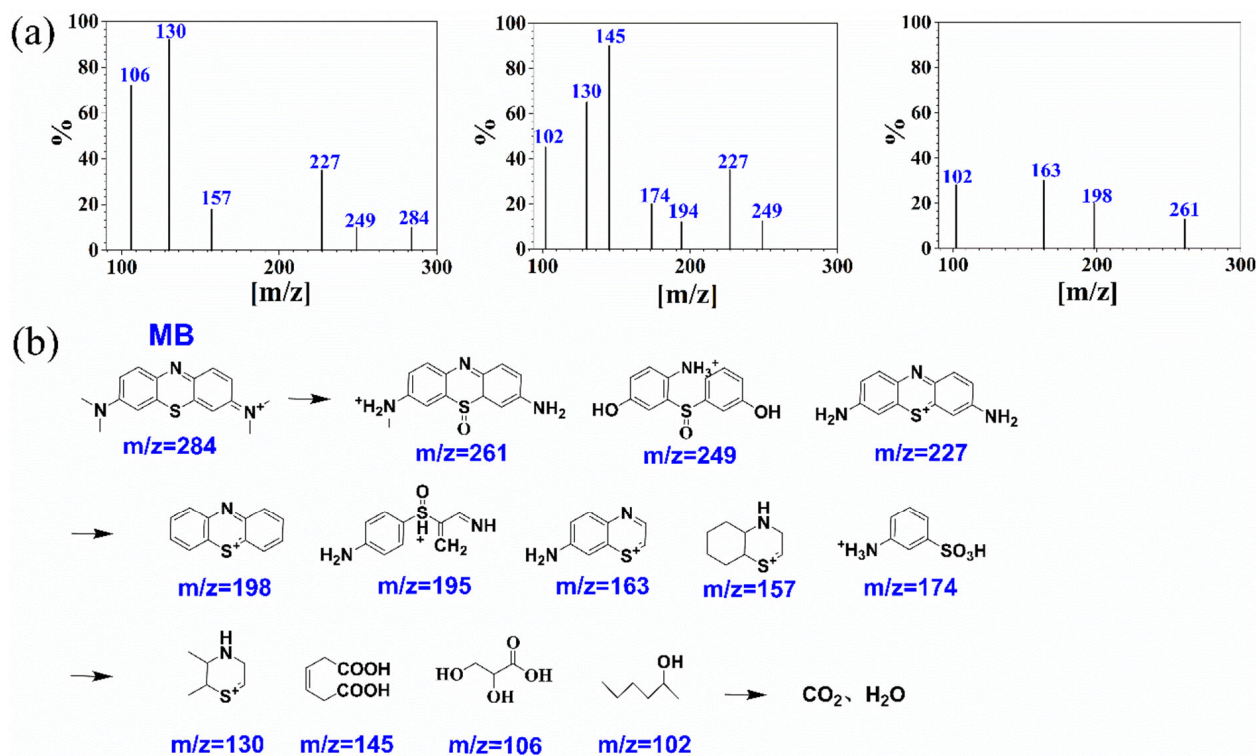
Figure 7. (**a**) Mass spectra of MB solutions at 30 min. (**b**) Proposed degradation pathway of MB.

Additionally, the efficiencies of MB degradation over **CuMoV(450)** and other metal oxides were compared, and the results are listed in Table 1. In terms of dosage, reaction time, and the efficiency of MB removal, **CuMoV(450)** exhibited the best degradation performance.

Table 1. Comparison of MB degradation efficiency over different metal oxides.

Catalyst	Dosage (mg)	[MB] (mM)	Time (min)	Efficiency (%)
Fe_2O_3@Y [41]	150	0.01	60	61.5
TiO_2 nanoparticles [42]	300	0.06	250	93.1
MnO_x-PP [43]	400	0.05	60	99.5
CuMoV(450)	80	0.01	30	95.9

2.3. Reduction of Cr(VI)

The catalytic reduction activity of **CuMoV(450)** was investigated by using $K_2Cr_2O_7$ as a Cr(VI) source and $NaBH_4$ as a reducing agent. The reduction progress was judged by monitoring the UV–vis absorption changes at 370 nm, which is the characteristic peak of the Cr(VI) solution [44]. Figure 8a indicates that neither $NaBH_4$ nor **CuMoV/CuMoV(450)** could reduce Cr(VI) to Cr(III), and the best result could be only achieved on condition that **CuMoV(450)** and $NaBH_4$ coexisted in the solution. In the $NaBH_4$-**CuMoV(450)** system, the yellow color of the Cr(VI) solution transformed into colorless in 2.0 min, illustrating that all the Cr(VI) was completely reduced to Cr(III) [44]. The stronger catalytic activity of **CuMoV(450)** indicates that the calcination treatment could evidently improve the catalytic activity of **CuMoV**.
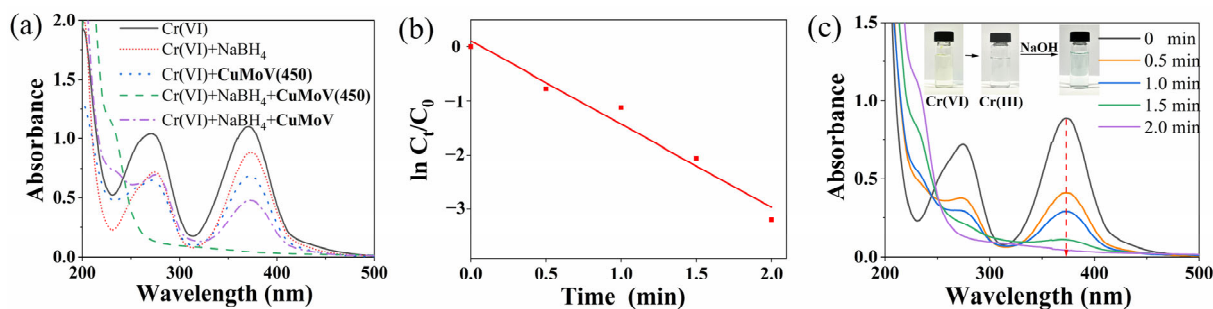
Figure 8. (**a**) Control experiments of Cr(VI) reduction, (**b**) The linear correlation between $\ln(C_t/C_0)$ and reaction time for Cr(VI) reduction over **CuMoV(450)**, (**c**) Time-varying UV–vis spectra of Cr(VI) reduction over **CuMoV(450)** under optimum conditions. $[K_2Cr_2O_7]$ = 0.1 mM, $[NaBH_4]$ = 8 mM, **CuMoV/CuMoV(450)** dosage = 40 mg, $[NaOH]$ = 1 M.

The catalytic reduction of Cr(VI) was affected by the dosage of **CuMoV(450)**, the initial concentration of Cr(VI) and $NaBH_4$, and the corresponding experimental results are given in Figure S5. Under the optimum conditions, the reduction rate of Cr(VI) was 96.5% in 2 min. The pseudo-first-order reaction kinetic model was taken to calculate the K_{app} and R^2, and the dates were 1.536 min^{-1} and 0.958, respectively (Figure 8b). The changes in the UV–vis spectra indicate that the characteristic absorption peak of the Cr(VI) solution gradually weakened until it disappeared (Figure 8c). Furthermore, the colorless supernatant solution obtained after Cr(VI) reduction turned green with the treatment of NaOH, authenticating the production of the Cr(III) complex (hexahydroxochromate(III)) [45]. The above-mentioned experimental phenomena confirmed the successful reduction of toxic Cr(VI) to nontoxic Cr(III).

The mechanism of the catalytic reduction was closely related to the electron donor ($NaBH_4$) and electron acceptor (Cr(VI)). At first, $NaBH_4$ disassociated to generate BH_4^- ions, which react with water to yield BO_2^-, H^+, and e^- (Equation (13)). Then, **CuMoV(450)** mediated the transport of H^+ and e^- to Cr(VI) and pushed the completion of the reduction [44]. **CuMoV(450)** accepted electrons from $NaBH_4$ and then transferred to Cr(VI).

$$BH_4^- + 2H_2O \rightarrow BO_2^- + 8H^+ + 8e^- \tag{13}$$
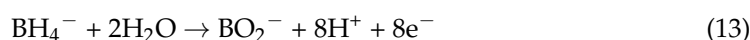
Table 2 presents the catalytic reduction abilities of **CuMoV(450)** and other mixed metal oxides. It is obvious that **CuMoV(450)** was more efficient than other catalysts with respect to lower $NaBH_4$ concentration and shorter time.

Table 2. Comparison of Cr(VI) reduction over different catalysts.

Catalyst	Dosage (mg)	[Cr(VI)] (mM)	[NaBH$_4$] (mM)	Time (min)	Efficiency (%)
CeVOS-3 [46]	15	0.3	7	4	60.0
2-AgMoOS [44]	40	0.1	200	24	96.6
CuMoV(450)	40	0.1	8	2	96.5

2.4. Recyclability

The recyclability of **CuMoV(450)** for MB degradation or catalytic reduction of Cr(VI) was investigated to assess its economic and practical value. It was tested three times consecutively and after each use, **CuMoV(450)** was simply filtered out from the reaction systems, washed with water and acetonitrile three times, and then dried overnight at room temperature. Figure 9a shows that **CuMoV(450)** could be reused for three cycles with a slight decrease in catalytic ability. Furthermore, the FT-IR spectra displayed in Figure 9b

reveal that no observable change could be found in the FT-IR spectra of the freshly prepared and the recycled **CuMoV(450)**. Such results not only confirm that **CuMoV(450)** is a stable and recyclable catalyst, but also suggest that **CuMoV(450)** has application potential in the field of environmental remediation.
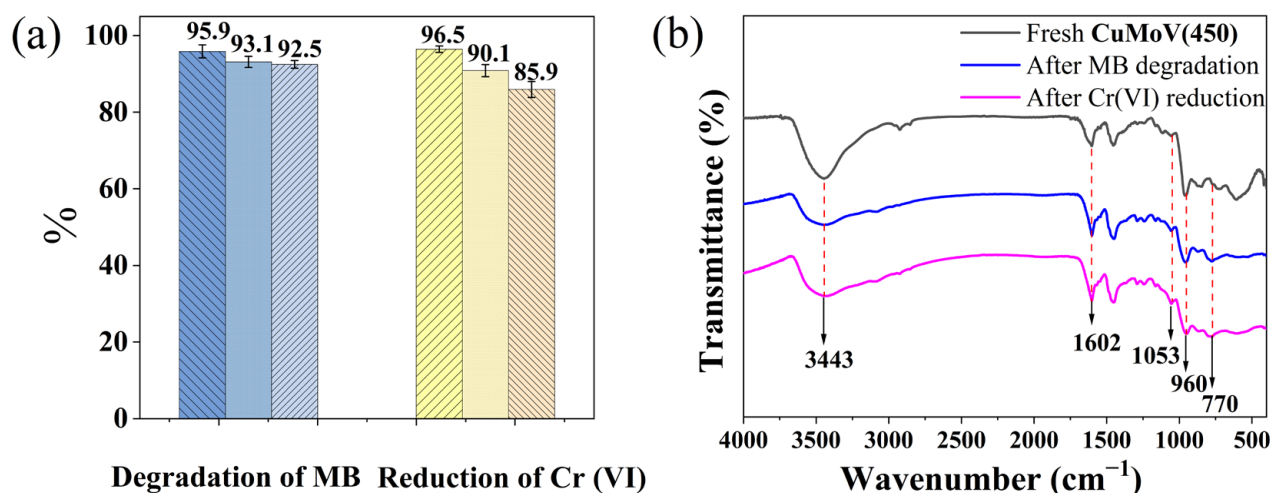
Figure 9. (**a**) MB degradation rate and Cr(VI) reduction rate in different recycle runs. (**b**) FT-IR spectra of **CuMoV(450)** before and after MB degradation/Cr(VI) reduction.

3. Experimental

3.1. Chemicals and Reagents

All the chemicals were analytical grade and purchased from Nanjing Wanqing reagent company (Nanjing, China). The deionized water was used in all the catalytic experiments.

3.2. Synthesis of *CuMoV* and *CuMoV(450)*

CuMoV was synthesized according to the literature method [47]. $Na_2MoO_4 \bullet 2H_2O$ (0.73 g, 3.0 mmol), NH_4VO_3 (0.35 g, 3.0 mmol), $CuSO_4 \bullet 5H_2O$ (0.75 g, 3.0 mmol), 2,2′-bipy (0.234 g, 1.5 mmol), $H_2C_2O_4 \bullet 2H_2O$ (0.19 g, 1.5 mmol), and H_2O (13.5 mL, 750 mmol) were mixed in a molar ratio of 2:2:2:1:1:500 and stirred for 2 h. The pH of the mixture was then adjusted to 4 using a dilute H_3PO_4 solution. The mixture was sealed in a 25 mL Teflon-lined autoclave and heated at 180 °C for 72 h. **CuMoV** were obtained as black rhombic blocky crystals after natural cooling to room temperature.

CuMoV was calcined at 450 °C for 2 h in a muffle and the obtained material was denoted as **CuMoV(450)**, where 450 indicated the calcination temperature.

3.3. Chemical Analysis

The chemical structures of **CuMoV** and **CuMoV(450)** were analyzed by X-ray photo-electron spectroscopy (AXIS UltraDLD, Shimadzu, Kyoto, Japan), Fourier infrared spectroscopy (Bruker Vertex 80 FTIR spectrometer, Billerica, MA, USA), Scanning electron microscope (FEI Quanta 200, Hillsboro, OR, USA), and energy dispersive X-ray spectroscopy (Oxford X-Act, Abingdon, UK). XRD analysis was performed using a Rigaku XRD Ultima IV diffractometer (Rigaku, Tokyo, Japan) employing nickel-filtered Cu Kα radiation (wavelength 1.5406 Å) over a range of 5° < 2θ < 50°. Thermogravimetric analysis was performed using a CHY-1200 box furnace (Henan Chengyi Equipment Technology Co., Ltd., Zhengzhou, China). Fluorescence analysis was run with LS55 (PerkinElmer, Waltham, MA, USA). The intermediates of MB degradation were detected by HPLC-MS (Agilent 5975c, Santa Clara, CA, USA) in positive ion mode with m/z ranging from 50 to 800 with acetonitrile as the mobile phase. The UV–vis spectra for monitoring MB degradation

and Cr(VI) reduction were recorded on a TU-1901 UV–visible spectrophotometer (Beijing Purkinje General Instrument Co., Ltd., Beijing, China).

3.4. Catalytic Activities Evaluation

3.4.1. MB Degradation

The reaction was carried out by dispersing **CuMoV(450)** in an MB solution with the required dosage at 25 °C without external reagents or energy input. If necessary, the pH of the MB solution was adjusted by 0.1 M HCl or NaOH, and the original pH of the MB solution was 6.8. 3 mL samples were taken out at given time intervals, filtered with a 0.45 um filter, and immediately measured the temporal UV–vis spectral variations of the MB solution. The absorbance of the sample was monitored at 664 nm, and the degradation rate and the quasi-first-order rate constant K_{app} were calculated by the following Equations (14) and (15), respectively.

$$\text{Degradation rate} = (C_t/C_0) \times 100\% \tag{14}$$

$$\ln (C_t/C_0) = -K_{app}t \tag{15}$$

where C_0 and C_t represent the initial concentration and the concentration at t time, respectively. All experiments were repeated three times and data were averaged.

3.4.2. Cr(VI) Reduction

After the specified quantity of **CuMoV(450)** and freshly prepared NaBH$_4$ solution with a concentration of 10 mM were added to the K$_2$Cr$_2$O$_7$ solution (0.1 mM, 50 mL), the reduction began. Then, 3 mL samples were taken out at given time intervals, filtered with a 0.45 um filter and immediately measured the temporal UV–vis spectral variations of the Cr(VI) solution. The reduction rate and the pseudo-first-order rate constant K_{app} were calculated by the following Equations (16) and (17), respectively.

$$\text{Reduction rate} = (C_t/C_0) \times 100\% \tag{16}$$

$$\ln (C_t/C_0) = -K_{app}t \tag{17}$$

where C_0 and C_t represent the initial concentration and the concentration at t time, respectively. All experiments were repeated three times and data were averaged.

4. Conclusions

In summary, a mixed metal oxide **CuMoV(450)** built on a POMOF [Cu(2,2′-bipy)][Cu(2,2′-bipy)$_2$]$_2$[PMo$^{VI}_8$V$_1^V$V$_3^{IV}$O$_{40}$(V^{IV}O)$_2$]•2H$_2$O (**CuMoV**) by calcination at 450 °C was successfully yielded. **CuMoV(450)** showed significantly improved activities for the heterogeneous catalytic degradation of MB and catalytic reduction of Cr(VI) compared to the parent **CuMoV**. Whether in MB degradation or Cr(VI) reduction, only a slight loss in the catalytic activities occurred after the third cycle. The catalytic activities of **CuMoV(450)** were superior to the other corresponding metal oxide catalysts in the heterogeneous catalytic degradation of MB and catalytic reduction of Cr(VI). What is even more commendable is that **CuMoV(450)** possessed both catalytic activities and excellent performance. The easy preparation, good stability, reusability, and excellent multi-functional performances make **CuMoV(450)** promising from both environmental and economic aspects. This is the first mixed metal oxide derived from a POMOF that was used as a catalyst in both oxidation and reduction. Furthermore, this work provides a clue to design new green heterogeneous catalysts based on POMOF for wastewater treatment.

Author Contributions: Investigation, Z.-Q.L.; data curation, J.-Y.L.; supervision, X.M.; project administration, B.-L.F. All authors have read and agreed to the published version of the manuscript.

Data Availability Statement: Data are contained within the article and Supplementary Materials.

Conflicts of Interest: The authors declare no conflicts of interest.

References

1. Chen, Y.H.; Liu, Z.L.; Liu, Z.S.; Feng, P.Z. Enhanced catalytic degradation of organic pollutant by $AgBiO_3$ with metastable lattice. *Mater. Res. Bull.* **2022**, *153*, 111882. [CrossRef]

2. Fu, B.; Sun, H.; Liu, J.; Zhou, T.; Chen, M.; Cai, Z.; Hao, D.; Zhu, X. Construction of MIL-125-NH_2@$BiVO_4$ composites for efficient photocatalytic dye degradation. *ACS Omega* **2022**, *7*, 26201–26210. [CrossRef] [PubMed]

3. Liu, J.; Dai, Q.H.; Xiao, R.X.; Zhou, T.T.; Han, J.L.; Fu, B. Immobilization of $ZnIn_2S_4$ on sodium alginate foam for efficient hexavalent chromium removal. *Int. J. Biol. Macromol.* **2023**, *236*, 123848. [CrossRef] [PubMed]

4. Akram, M.Y.; Hameed, M.U.; Akhtar, N.; Ali, S.; Maitlo, I.; Zhu, X.Q.; Nie, J. Synthesis of high performance Ni_3C-Ni decorated thermally expanded reduced graphene oxide (TErGO/Ni_3C-Ni) nanocomposite: A stable catalyst for reduction of Cr(VI) and organic dyes. *J. Hazard. Mater.* **2019**, *366*, 723–731. [CrossRef]

5. Naz, M.; Rafiq, A.; Ikram, M.; Haider, A.; Ahmad, S.O.A.; Haider, J.; Naz, S. Elimination of dyes by catalytic reduction in the absence of light: A review. *J. Mater. Sci.* **2021**, *56*, 15572–15608. [CrossRef]

6. Chen, H.H.; Motuzas, J.; Martens, W.; Costa, J.C.D. Degradation of orange II dye under dark ambient conditions by MeSrCuO (Me = Mg and Ce) metal oxides. *Sep. Purif. Technol.* **2018**, *205*, 293–301. [CrossRef]

7. Leng, Y.; Liu, J.X.; Zhang, Z.H.; Chen, H.; Zhang, P.F.; Dai, S. Polyoxometalates as bifunctional templates: Engineering metal oxides with mesopores and reactive surfaces for catalysis. *J. Mater. Chem. A* **2019**, *7*, 27297–27303. [CrossRef]

8. Zhong, W.; Jiang, T.; Dang, Y.L.; He, J.K.; Chen, S.Y.; Kuo, C.H.; Kriz, D.; Meng, Y.T.; Meguerdichian, A.G.; Suib, S.L. Mechanism studies on methyl orange dye degradation by perovskite-type $LaNiO_{3-\delta}$ under dark ambient conditions. *Appl. Catal. A-Gen.* **2018**, *549*, 302–309. [CrossRef]

9. Recepoglu, Y.K.; Goren, A.Y.; Orooji, Y.; Vatanpour, V.; Kudaibergenov, N.; Khataee, A. Polyoxometalate-based hybrid composites in multi-functional wastewater treatment applications. *J. Water Process. Eng.* **2023**, *53*, 103863. [CrossRef]

10. Huang, B.; Ma, Y.T.; Xiong, Z.L.; Xiao, Z.C.; Wu, P.F.; Jiang, P.; Liang, M.H. Polyoxometalate-derived $Ir/WO_x/rGO$ nanocomposites for enhanced electrocatalytic water splitting. *Energy Environ. Mater.* **2021**, *4*, 681–686. [CrossRef]

11. Dai, D.L.; Qiu, J.H.; Xia, G.L.; Tang, Y.; Liu, Q.Y.; Li, Y.X.; Fang, B.Y.; Yao, J.F. Metal-organic framework templated Z-scheme $ZnIn_2S_4/Bi_2S_3$ hierarchical heterojunction for photocatalytic H_2O_2 production from wastewater. *Small* **2024**, *20*, 2403268. [CrossRef] [PubMed]

12. Zhang, S.W.; Ou, F.X.; Ninga, S.; Cheng, P. Polyoxometalate-based metal-organic frameworks for heterogeneous catalysis. *Inorg. Chem. Front.* **2021**, *8*, 1865–1899. [CrossRef]

13. Zhang, Y.D.; Lin, B.P.; Wang, J.C.; Han, P.; Xu, T.; Sun, Y.; Zhang, X.Q.; Yang, H. Polyoxometalates@metal-organic frameworks derived porous MoO_3@CuO as electrodes for symmetric all-solid-state supercapacitor. *Electrochim. Acta* **2016**, *191*, 795–804. [CrossRef]

14. Tang, Y.J.; Gao, M.R.; Liu, C.H.; Li, S.L.; Jiang, H.L.; Lan, Y.Q.; Han, M.; Yu, S.H. Porous molybdenum-based hybrid catalysts for highly efficient hydrogen evolution. *Angew. Chem. Int. Ed.* **2015**, *54*, 12928–12932. [CrossRef] [PubMed]

15. Ma, W.J.; Li, Y.S.; Gao, S.T.; Cui, J.X.; Qu, Q.L.; Wang, Y.L.; Huang, C.B.; Fu, G.D. Self-healing and superwettable nanofibrous membranes with excellent stability toward multifunctional applications in water purification. *ACS Appl. Mater. Inter.* **2020**, *12*, 23644–23654. [CrossRef]

16. Wang, Y.; Feng, Y.; Jiang, J.; Yao, J. Designing of recyclable attapulgite for wastewater treatments: A review. *ACS Sustain. Chem. Eng.* **2019**, *7*, 1855–1869. [CrossRef]

17. Clarke, R.C.; Latham, K.; Rix, C.J.; Hobday, M. Heterocyclic amine derivatives of zinc organophosphonates. *Chem. Mater.* **2004**, *16*, 2463–2470. [CrossRef]

18. Ibrahim, A.A.; Hassan, S.M.; Mannaa, M.A. Mesoporous tin oxide-supported phosphomolybdic acid as high performance acid catalysts for the synthesis of hydroquinone diacetate. *Colloid. Surf. A* **2020**, *586*, 124248. [CrossRef]

19. Farhadi, S.; Zareisahamieh, R.; Zaidi, M. $H_6GeMo_{10}V_2O_{40} \bullet 16H_2O$ nanoparticles prepared by hydrothermal method: A new and reusable heteropoly acid catalyst for highly efficient acetylation of alcohols and phenols under solvent-free conditions. *J. Brazil. Chem. Soc.* **2011**, *22*, 1323–1332. [CrossRef]

20. Fei, F.; Zhou, H.; Kang, M. POM-derived $MoO_3/CoMoO_4$ mixed oxides directed by glucose for high-performance supercapacitors. *New J. Chem.* **2022**, *46*, 16914–16921. [CrossRef]

21. Akyüz, S.; Akyüz, T.; Ozer, N.M. FT-IR spectroscopic investigations of benzidine and bipyridyls adsorbed on diatomite from Anatolia. *J. Mol. Struct.* **2001**, *565*, 493–496. [CrossRef]

22. Daichi, I.; Masaru, M. Characterization of magnesium-intercalated V2O5/carbon composites. *Solid State Ionics* **2003**, *161*, 173–180. [CrossRef]

23. Guhergul, U.; Busra, Y.; Sevket, E.O.; Aktas, S. Double vanadyl-carrying phenanthroline complexes: Template synthesis and DFT study. *Chem. Pap.* **2020**, *74*, 1881–1889. [CrossRef]

24. Li, Y.R.; Ren, H.; Jiao, Q.J. Preparation and characterization of MoO_3 with different morphologies. *Ferroelectrics* **2018**, *527*, 113–118. [CrossRef]

25. Abo-Naf, S.M.; El-Amiry, M.S.; Abdel-Khalek, A.A. FT-IR and UV-Vis optical absorption spectra of c-irradiated calcium phosphate glasses doped with Cr_2O_3, V_2O_5 and Fe_2O_3. *Opt. Mater.* **2008**, *30*, 900–909. [CrossRef]

26. Singh, M.; Kumar, P.; Sharma, R.K.; Reddy, G.B. Plasma assisted synthesis and growth mechanism of rare V_2O_5 nanostructured thin films. *J. Alloy. Compd.* **2017**, *690*, 532–541. [CrossRef]

27. Zhang, R.Y.; Zhang, A.L.; Cao, Y.H.; Wang, S.Y.; Dong, F.; Zhou, Y. Mo-doped carbon nitride homojunction to promote oxygen activation for enhanced photocatalytic performance. *Chem. Eng. J.* **2020**, *401*, 126028. [CrossRef]

28. Guo, F.; Liu, J.M.; Zhang, W.G.; Yu, Z.B.; Liu, Y.M.; Liang, W.; Cu, S.O. N-doped TiO_2 nanotube by a novel magnetron sputtering method and its photoelectric property. *Vacuum* **2019**, *165*, 223–231. [CrossRef]

29. Lee, G.J.; Manivel, A.; Batalova, V.; Mokrousov, G.; Masten, S.; Wu, J. Mesoporous microsphere of ZnS photocatalysts loaded with CuO or Mn_3O_4 for the visible-light-assisted photocatalytic degradation of orange II dye. *Ind. Eng. Chem. Res.* **2013**, *52*, 11904–11912. [CrossRef]

30. Periyayya, U.; Madhu, D.; Subramaniyam, K.; Son, H.; Lee, I.H. Enhanced cyclic performance initiated via an in situ transformation of Cu/CuO nanodisk to Cu/CuO/Cu2O nanosponge. *Environ. Sci. Pollut. R.* **2020**, *28*, 6459–6469. [CrossRef]

31. Wu, Q.H.; Zhang, P.K.; Kuo, D.H.; Wu, B.H.; Abdeta, A.B.; Su, Z.J.; Chen, L.Y.; Zelekew, O.A.; Lin, J.G.; Chen, X.Y. Activation of $Cu_3(MoO_4)_2(OH)_2$ with the hydrazine-driven cation reduction into a highly efficient catalyst for the reduction of organic dyes and heavy metals ion $Cu_3(MoO_4)_2(OH)_2$. *J. Environ. Chem. Eng.* **2023**, *11*, 109974. [CrossRef]

32. Jiang, W.; Xiao, J.; Dong, L.; Wang, C.; Li, H.P.; Luo, Y.P.; Zhu, W.S.; Li, H.M. Polyoxometalate-based poly(ionic liquid) as a precursor for superhydrophobic magnetic carbon composite catalysts toward aerobic oxidative desulfurization. *Acs. Sustain. Chem. Eng.* **2019**, *7*, 15755–15761. [CrossRef]

33. Kumar, M.; Ansari, M.N.M.; Boukhris, I.; Al-Buriahi, M.S.; Alrowaili, Z.A.; Alfryyan, N.; Thomas, P.; Vaish, R. Sonophotocatalytic dye degradation using $rGO-BiVO_4$ composites. *Glob. Chall.* **2022**, *6*, 2100132. [CrossRef] [PubMed]

34. Wang, H.Q.; Liang, Z.D.; Liu, C.; Zhu, L.S.; Xu, Y.T.; Zhou, L.; Yan, B. Construction of K and Tb Co-doped MnO_2 nanoparticles for enhanced oxidation and detoxication of organic dye waste. *Chemosphere* **2022**, *297*, 134104. [CrossRef]

35. Zeng, C.; Hu, Y.M.; Huang, H.W. $BiOBr_{0.75}I_{0.25}/BiOIO_3$ as a novel heterojunctional photocatalyst with superior visible-light-driven photocatalytic activity in removing diverse industrial pollutants. *ACS Sustain. Chem. Eng.* **2017**, *5*, 3897–3905. [CrossRef]

36. Chen, H.H.; Fu, W.; Xing, Y.L.; Zhang, J.X.; Ku, J.G. Engineering $SrCu_xO$ composition to tailor the degradation activity toward organic pollutant under dark ambient conditions. *Environ. Sci. Pollut. R.* **2019**, *26*, 16449–16456. [CrossRef]

37. Zhang, Y.M.; Zhang, N.S.; Wang, T.T.; Huang, H.T.; Chen, Y.; Li, Z.S.; Zou, Z.G. Heterogeneous degradation of organic contaminants in the photo-Fenton reaction employing pure cubic β-Fe_2O_3. *Appl. Catal. B-Environ.* **2019**, *245*, 410–419. [CrossRef]

38. He, Q.; Liao, X.G.; Li, G.; He, Y.X.; Shen, J. Synthesis of cubic Mn_2O_3 and its catalytic performance in activating peroxymonosulfate for degradation of MB. *Chem. Phys.* **2023**, *571*, 111912. [CrossRef]

39. Zhao, J.J.; Wang, X.X.; Dai, P. Syntheses, structures and photocatalysis properties of two Cu(II)-based coordination polymers based on flexible tricarboxylate ligand. *J. Mol. Struct.* **2021**, *1235*, 130220. [CrossRef]

40. Hong, W.W.; Lu, L.; Yue, M.; Huang, C.C.; Muddassir, M.; Sakiyama, H.; Wang, J. A 3D 8-connected bcu topological metal-organic framework built by trinuclear Cd(II) units: Photocatalysis and LC-MS studies. *Polyhedron* **2021**, *211*, 115571. [CrossRef]

41. Duan, Y.L.; Zhang, R.X.; Han, P.F.; Wong, N.H.; Sunarso, J.; Liu, S.M.; Yu, J. Fabricating an adsorbent and micro-nano bubble catalyst through confining maghemite in the β cage of NaY zeolite. *Chemosphere* **2024**, *350*, 141103. [CrossRef] [PubMed]

42. Cui, X.D.; Li, P.C.; Lei, H.; Tu, C.; Wang, D.L.; Wang, Z.; Chen, W.P. Greatly enhanced tribocatalytic degradation of organic pollutants by TiO_2 nanoparticles through efficiently harvesting mechanical energy. *Separ. Purif. Technol.* **2022**, *289*, 120814. [CrossRef]

43. Zheng, J.Y.; He, J.D.; Han, C.B.; Huang, G.Y.; Sun, B.C.; Zhao, W.K.; Wen, K.; Wang, Y.S.; Sun, L.; Si, J.H.; et al. Adsorption-enhanced catalytic oxidation for long-lasting dynamic degradation of organic dyes by porous manganese-based biopolymeric catalyst. *Int. J. Biol. Macromol.* **2023**, *237*, 124152. [CrossRef] [PubMed]

44. Abdeta, A.B.; Sun, H.Z.; Guo, Y.B.; Wu, Q.H.; Zhang, J.B.; Yuan, Z.H.; Lin, J.G.; Chen, X.Y. A novel AgMoOS bimetallic oxysulfide catalyst for highly efficiency catalytic reduction of organic dyes and chromium (VI). *Adv. Powder. Technol.* **2021**, *32*, 2856–2872. [CrossRef]

45. Bashir, M.S. Benign fabrication process of hierarchal porous polyurea microspheres with tunable pores and porosity: Their Pd immobilization and use for hexavalent chromium reduction. *Chem. Eng. Res. Des.* **2021**, *175*, 102–114. [CrossRef]

46. Zhang, P.K.; Lai, Y.J.; Dai, X.H.; Xu, Y.Z.; Wu, X.R.; Yang, B.Q.; Kuo, D.H.; Lu, D.F.; Wu, Q.H.; Mosisa, M.T.; et al. Hydrazine-driven cation valence regulation and defect engineering in $CeVO_4$ for highly efficient reduction of organic dyes and heavy metal pollutants in the dark. *J. Environ. Chem. Eng.* **2024**, *12*, 111831. [CrossRef]

47. Cui, J.W.; Cui, X.B.; Xu, J.N.; Yu, H.H.; Xu, J.Q.; Duan, W.J.; Wang, T.G. Two new polyoxometalate tri-supported transition metal complexes constructed from bi-capped Keggin molybdenum-vanadium clusters and copper complex fragments. *J. Mol. Struct.* **2008**, *891*, 35–39. [CrossRef]